Bulletin of the Seismological Society of America, Vol. 104, No. 3, pp. 1088–1099, June 2014, doi: 10.1785/0120130133

Temporal Variations of Seismic Velocity at Paradox Valley, Colorado, Using Passive Image Interferometry

by Arantza Ugalde, Beatriz Gaite, and Antonio Villaseñor

Abstract Passive image interferometry is applied to monitor seismic velocity changes in Paradox Valley (southwestern Colorado). For this purpose, we analyzed short-period vertical-component continuous recordings of seismic ambient noise from the Paradox Valley seismic network from January 2011 to March 2012. Continuous, high-pressure fluid injection activities at depths of about 4.8 km are occurring in this region. We computed the autocorrelation functions using band-pass-filtered data in the frequency ranges 0.2–0.5, 0.5–1, 1–2, and 2–8 Hz. The relative perturbations of the background seismic velocity were estimated using the stretching technique and the moving window cross-spectral analysis assuming a uniform velocity change in space. A clear seasonal trend of the relative velocity variations is observed, with the higher amplitudes corresponding to the lower frequency bands. The long-term variations of the relative velocity at low frequencies show an annual period that peaks in winter. For higher frequencies, semiannual seasonal variations are observed. A comparison of our results with the horizontal differential displacements for two pair of Global Positioning System stations, meteorological time series, and water-table measurements allows us to conclude that hydrologic loading can explain a large fraction of the observed long-term relative velocity variations in the area. No correlation is observed between the short-term relative velocity variations and the cumulative number of induced earthquakes in the region, nor with the average brine injection rates. More high-quality data from a denser network would be necessary to make a detailed interpretation of the short-term variations in relation to the fluid injection activity in the Paradox Valley region.

Introduction

Noise-based seismic monitoring techniques have a great potential to study the Earth's interior at different scales in space and time. The main principle behind these methods is the relationship between the cross correlation of random wavefields and the Green's function (GF) between two points, which has been demonstrated both theoretically and experimentally in various fields of wave physics (e.g., Larose *et al.*, 2006; Campillo *et al.*, 2011). Furthermore, it has been demonstrated theoretically that the cross-correlation function (CCF) between two seismic records result in the retrieval of the full GF (e.g., Wapenaar and Fokkema, 2006). In the limit as the two stations are coincident, the cross correlogram becomes the autocorrelogram for a single station that yields the seismic response for a coincident source and receiver position (e.g., Sens-Schönfelder and Wegler, 2011). Because of the surface nature of most of the noise sources in the Earth, the surface-wave part of the GF is most easily extracted from noise correlations (e.g., Shapiro *et al.*, 2005). However, it has also been demonstrated that the coda part of the GF can be reconstructed from the autocorrelation function (ACF) that, in theory, contains information on the scattered field. The coda portion of ambient noise auto and CCFs, which reflects the complex structure of the medium (Sato, 2010; Margerin and Sato, 2011), has been used to detect temporal variations of seismic velocity. The technique used here is called passive image interferometry (PII, Sens-Schönfelder and Wegler, 2006; Wegler and Sens-Schönfelder, 2007) and combines the well-established procedure of estimating the GFs between station pairs by correlating the seismic noise recordings of both sensors (e.g., Shapiro and Campillo, 2004; Wapenaar *et al.*, 2010) with coda wave interferometry (e.g., Poupinet *et al.*, 1984; Snieder, 2006).

Recent works have demonstrated that PII is able to detect velocity changes below 0.1%, which are unnoticeable from travel-time analysis of first arrivals, and they are associated to different tectonic (such as the closure and opening of cracks due to earthquakes) and nontectonic (rainfall or atmospheric pressure) causes (Sens-Schönfelder and Wegler, 2011). PII applications cover the detection of changes in fault zones (e.g., Wegler and Sens-Schönfelder, 2007; Brenguier *et al.*, 2008a; Ohmi *et al.*, 2008; Wegler *et al.*, 2009; Chen *et al.*, 2010; Maeda *et al.*, 2010; Hobiger *et al.*, 2012; Minato *et al.*,

2012; Ueno *et al.*, 2012), volcano monitoring (e.g., Brenguier *et al.*, 2008b; Duputel *et al.*, 2009; Mordret *et al.*, 2010; Anggono *et al.*, 2012), and even the analysis of velocity changes in the lunar subsurface (Sens-Schönfelder and Larose, 2008). Injection and movement of fluids in geologic formations causes changes in seismic velocities and attenuation, resulting in changes in seismic-wave scattering and propagation (Zhou *et al.*, 2010). The changes in seismic velocities can be associated with changes in fluid saturation, increase in pore pressure, or the opening or enlargement of cracks due to the injection process. The capability of PII to monitor CO_2 storage in deep saline formations is also being explored in Hontomín, northern Spain (Ugalde *et al.*, 2013).

A continuous, high-pressure, long-term deep fluid injection is presently occurring in Paradox Valley (southwestern Colorado). In this study, we apply PII to monitor velocity changes in this region and assess their causes using continuous ambient noise seismic recordings from the Paradox Valley (PV) seismic network.

The Paradox Valley Unit

Paradox Valley is an ~40 km long, ~4–7 km wide region located in the northeastern part of Paradox basin within the Colorado Plateau (Fig. 1). It is a graben formed by a collapsed diapiric salt anticline bounded on the northeast and southwest by a series of normal faults. The shallow, saline-saturated Paradox Valley aquifer is a natural source of excess salinity in the Dolores River that crosses perpendicular to the valley axis. To reduce the salinity in the Dolores River, a tributary of the Colorado River, the U.S. Bureau of Reclamation is operating the Paradox Valley Unit (PVU), a facility to extract aquifer brine from several shallow wells located along the river that is then injected under high pressure into a 4.8 km deep well at the edge of the valley. The injection well was sited to optimize fluid migration into and along inactive northwest-trending, northeast-dipping basement faults on the northeast flank of the Wray Mesa structural trend (Ake *et al.*, 2005; United States Bureau of Reclamation [USBR], 2012).

Seismicity induced by injection is monitored by the PV seismic network, which initially consisted of 15 short period (T_0 = 1 Hz) seismic stations arranged around the injection well (Ake *et al.*, 2005). The network has been upgraded recently to 20 broadband stations, however, continuous recordings from the new broadband stations are not available yet (USBR, personal comm., 2013). Figure 1 shows the locations of the six old short-period stations for which high-quality archive data were still available. Because the continuous injection continued from 1996 to the end of 2011, PVU has emplaced more than 6×10^7 m^3 of fluid, and more than 5000 induced events have been located. According to the PV network seismic catalog, the largest induced earthquake had a local magnitude of 4.3 and occurred on 27 May 2000, whereas more than the 98.8% of the seismicity is below local magnitude 2.5. In order to keep seismicity at low, nondamaging levels, PVU has changed the injection strategies several times. At present, average injection rates are around 840 L/min with 20-day shutdowns every six months.

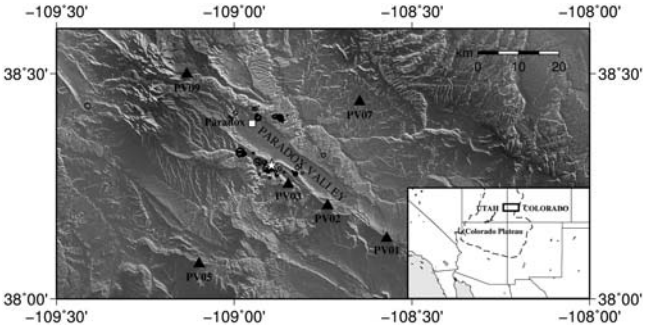

Figure 1. Map of the study area. Solid triangles show the seismic stations of the Paradox Valley (PV) seismic network used in the analysis. Epicenters of the induced earthquakes that occurred during 2011 are plotted with open circles. The open square indicates the location of the Paradox 2N meteorological station. The open star marks the location of the deep injection well. The map was drawn with Generic Mapping Tools (Wessel and Smith, 1998).

Induced seismicity at Paradox Valley is vertically confined to a depth range from 3.5 to 6 km below surface, and it occurs in two zones. The zone where most of the events are located is asymmetrically distributed around the deep well. A second zone is displaced around 8 km to the northwest of the injection well (Fig. 1). Ake *et al.* (2005) noted that seismically illuminated faults and fractures can accommodate only a few percent of the injected fluid. Therefore, numerous small fractures must be continuously opened to provide the remaining additional storage volume.

Data Set

We analyzed 15 months of continuous data from 1 January 2011 to 31 March 2012 recorded at PV seismic network. For this purpose, we downloaded the continuous vertical-component data available at the U.S. Geological Survey's (USGS) National Earthquake Information Center from the old short-period seismic stations that are still operating.

To assess the quality of the stations in terms of the ambient seismic noise levels recorded at each site, we computed the probability density functions of power spectral densities (PSDs) using PQLX software (McNamara and Boaz, 2011) for all the available stations of the PV seismic network. Figure 2 shows an example of the noise baseline envelopes obtained for 15 months of data for one seismic station. In this figure, the 5th, 50th, and 95th percentile of the PSD distribution are plotted together with the new high-noise and low-noise models of Peterson (1993). This procedure serves as a quality control of the network stations, because the computed PSDs consider all available data, including gaps and transient signals such as earthquakes or glitches. Noise levels are high at all the sites; and, after the analysis of the spectral data characteristics using this method, we focused on recordings from six stations located less than 35 km from the injection point (Fig. 1).

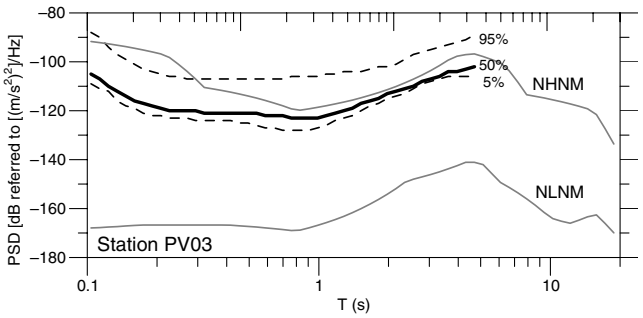

Figure 2. The power spectral density (PSD) distribution for station PV03. The median (50% percentile) for the HHZ component is plotted with a solid line. The dotted lines show the 5% (lower bound) and 95% (upper bound) percentiles of the PSD distribution. The gray lines represent the new high-noise model and new low-noise model of Peterson (1993).

Computation of the Noise Autocorrelation Functions

We calculated the noise ACFs for each station of the PV network using one-hour length continuous data following a processing scheme similar to Brenguier *et al.* (2008b). We removed the mean and trend and deconvolved the instrument response. Data were then band-pass filtered over the 0.2–0.5, 0.5–1, 1–2, and 2–8 Hz frequency bands and whitened. To normalize the seismic noise in time domain, we applied a one-bit normalization. Finally, we computed the autocorrelation functions and averaged the ACFs over 24 hr. The time derivative of the ACF was not computed, and the GF was approximated by the ACF itself, because the derivation procedure would only introduce a phase shift that would not affect the detection of velocity variations in the emerged signals (Sabra *et al.*, 2005).

Figure 3 shows an example of the evolution of the one-day averaged vertical-component autocorrelation functions for station PV05 in the frequency ranges 0.2–0.5 and 0.5–1 Hz for the entire time period analyzed here. The late phases of ACFs are coherent over different days.

Estimation of the Relative Velocity Changes

The relative perturbations of the background seismic velocity ($\delta v/v$) can be estimated, to a first order approximation, from the relative travel-time shift ($\delta\tau/\tau$) of the autocorrelation function with respect to a reference ACF. With the stretching technique (Sens-Schönfelder and Wegler, 2006) the time axis on the current ACF is stretched to get the best cross correlation with the reference ACF. The best-fitting stretching ratio is taken as an estimate of the relative velocity change. Another method for the retrieval of the relative velocity variations is the moving window cross-spectral (MWCS) analysis (Poupinet *et al.*, 1984) that consists of measuring the travel-time difference between two waveforms in each time window by fitting the phase differences in the frequency domain. Theoretical and laboratory studies have shown that the stretching method is more stable to fluctua-

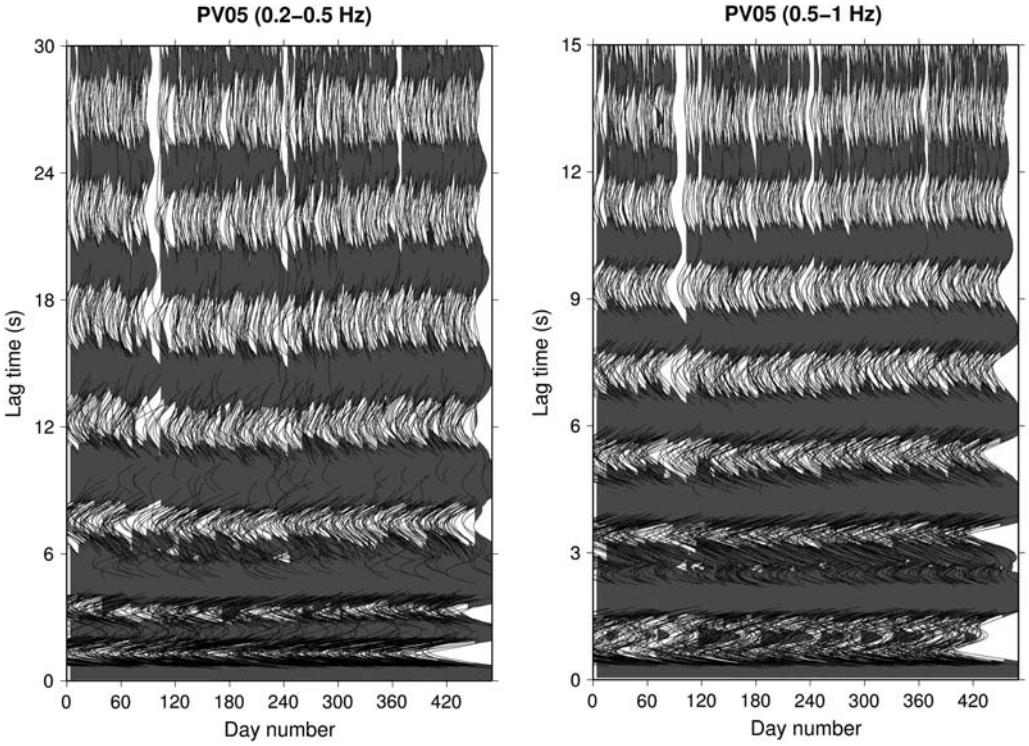

Figure 3. One-day averaged autocorrelation function (ACF) for station PV05 and the frequency ranges 0.2–0.5 Hz (left panel) and 0.5–1 Hz (right panel) during the period 1 January 2011 to 31 March 2012. White spaces at some days are caused by unavailable data. Note the different time lag scales in the different frequency ranges.

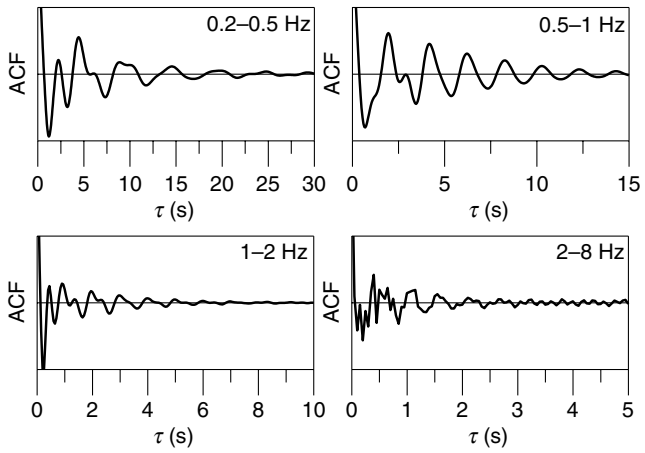

Figure 4. Reference autocorrelation functions for station PV09 in the period 1 January 2011 to 31 March 2012 for different frequency ranges from 0.2 to 8 Hz. Note the different time lag scales in the different frequency ranges.

tions in noise than the MWCS (Hadziioannou *et al.*, 2009); however, Zhan *et al.* (2013) have demonstrated that the temporal variability of noise frequency content at different time scales may cause apparent velocity changes if the stretching method is used. In this work, we apply both methods to diagnose the possible bias in the results introduced by the methodology in Paradox Valley.

The Stretching Technique

The stretching technique (Lobkis and Weaver, 2003; Sens-Schönfelder and Wegler, 2006) allows estimation of the relative time shifts by maximizing the correlation coefficient between the reference correlation function and a resampled version by $\tau(1-\varepsilon)$ of the current ACF for a range of ε, in which ε is called the stretching factor. For a uniform velocity change in space, $\delta v/v = -\delta\tau/\tau = \varepsilon$, and the relative velocity change is then given by $\delta v/v = \varepsilon_{\max}$, in which $\varepsilon_{\max}$ is the stretching factor ε that results in the best correlation coefficient between the current and the reference ACF.

Reference autocorrelation functions are calculated by stacking all daily ACFs for each station. Figure 4 shows an example of the reference ACFs for station PV09 of the PV network for all the studied frequency bands. The daily velocity variations are estimated for selected coda time windows of the ACFs. To automate the process, we adapted the time-window length to different frequency ranges. We considered coda windows with length of three periods starting at time lags equal to two periods, in which the periods are taken from the lowest frequency in the respective frequency band. The lower lag time limit is chosen to exclude scattered waves close to the receiver, and the upper limit corresponds to the time when the coherence in the coda decreases. These criteria yield the following time limits of the windows: 10–25 s for 0.2–0.5 Hz; 4–10 s for 0.5–1 Hz; 2–5 s for 1–2 Hz; and 1–2.5 s for 2–8 Hz. In this case, the upper extent of the time window is 2.5 times the lower extent. Finally, the daily relative velocity variations were determined using the grid-search stretching technique for 1000 trials of ε in a range from -5% to 5% ($\Delta\varepsilon = 0.01\%$).

The Moving Window Cross-Spectral Analysis

Similarly to the stretching technique, the MWCS method also requires the computation of a reference ACF. Then, the cross spectrum between the current and reference ACF for a series of overlapping time windows is computed and the spectral phase shift at different frequencies is measured. For each small time window, the time delay between the current and the reference ACF can be found by a weighted linear regression of the phase of the cross spectrum within the frequency range of interest. By repeating this procedure for all the small time windows considered, the time delay as a function of time along the ACF can be estimated. Then, the resulting velocity perturbation can be obtained as the slope of a linear regression applied to the time-delay measurements. This procedure assumes that the seismic-wave propagation velocity is perturbed homogeneously within the studied media. The computational details of the MWCS technique are fully described in Clarke *et al.* (2011). We used 50% overlapping, one-period-length lag-time windows for the analysis, within the same time limits as for the stretching technique.

Results

Figure 5b shows an example of the daily temporal changes of $\delta v/v$ obtained for station PV03 in the frequency range 0.5–1 Hz, between 4 and 10 s lapse time, using the stretching technique. Only measurements with best stretching coefficients $\varepsilon_{\max}$ that result in correlation coefficients greater that 0.7 are kept. Vertical error bars mark the standard deviation of independent measurements in three consecutive time windows (4–6, 6–8, and 8–10 s). It can be observed that the correlation coefficients between the current and reference ACF are high, with most of the values above 0.9; however, the measures are unstable. The daily velocity variations can be stabilized by averaging the ACFs over several days. We used smoothing lengths of 30 days with a one day moving window and plotted the results with a solid line in Figure 5b. Figure 5c shows the relative velocity variations obtained independently for the 4–6 and 8–10 s time windows along the ACF using the stretching technique. The late part of the ACF produces smaller relative velocity changes than the early one. A similar behavior was observed by Sens-Schönfelder and Wegler (2006) in the Merapi volcano and by Minato *et al.* (2012) after the Tohoku earthquake in Japan using the same technique; they interpreted their results in terms of the sensitivity of coda waves to depth-dependent velocity perturbations. However, according to Zhan *et al.* (2013), these observations may also be an evidence for apparent velocity changes caused by the stretching method that makes the late

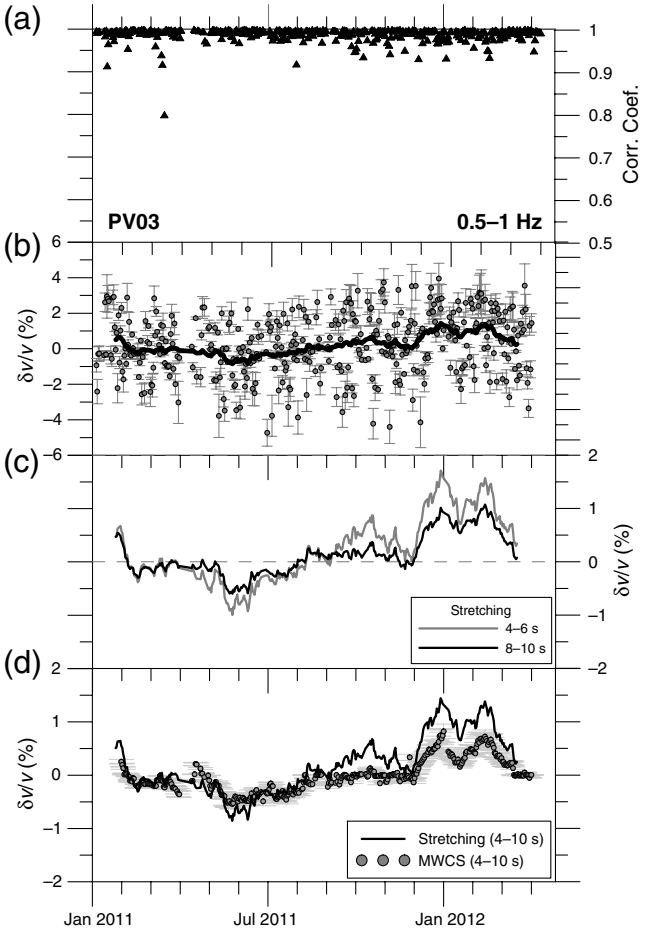

Figure 5. Relative velocity variations at station PV03 for the frequency range 0.5–1 Hz in the period 1 January 2011 to 31 March 2012: (a) correlation coefficient using the stretching technique; (b) daily (gray dots) and 30-day averaged (solid line) velocity variations using the stretching technique (vertical bars plot the estimated standard deviation for three nonoverlapping time windows in the interval 4–10 s); (c) velocity variations using the stretching method for the time windows 4–6 s (gray line) and 8–10 s (black line) along the ACF; and (d) comparison of the estimated velocity variations using the stretching method (solid line) and the moving window cross-spectral (MWCS) technique (gray dots) with their corresponding error bars.

part of the ACFs produce smaller relative velocity changes than the early part. For this reason, we also applied the MWCS technique to the data. Figure 5d shows a comparison of the relative velocity variations obtained using the stretching technique and the MWCS method for the 4–10 s time window along the ACF. The stretching technique causes up to 0.5% apparent velocity increase with respect to the MWCS method.

Figure 6 presents the relative velocity changes measured over 15 months (January 2011 to March 2012) in the Paradox Valley region in four different frequency ranges: 0.2–0.5, 0.5–1, 1–2, and 2–8 Hz for stations PV03 and PV05. Results in each frequency range are very similar among all the analyzed stations of the PV network for the frequency bands from 0.2 to 1 Hz. Results differ for the higher frequency bands, for which coda waves sample a shallower region close to each station. When comparing the results obtained using the stretching method and the MWCS technique, it can be observed that the relative velocity variations follow a similar trend, although the amplitude of the oscillation is greater if the stretching method is used. Velocity varies at different time scales at all frequencies. In order to better distinguish the short-term variations, we plotted in Figure 7 (left) one example of the long-term variations that were computed by means of a seventh-order polynomial fitting procedure of the raw data (e.g., Brenguier *et al.*, 2008b).

Discussion

Seasonal Velocity Changes

A clear seasonal trend of the relative velocity changes is observed in Figure 7 (left) at all frequencies. The amplitude of this variation is especially stronger for the lower analyzed frequency bands, and it is in the order of ±1% in the frequency range 0.2–0.5 Hz, ±0.5% for 0.5–1 Hz, ±0.25% for 1–2 Hz, and ±0.1% at higher frequencies. The observed long-term variations of the relative velocity at low frequencies show an annual period with a relative velocity peak in winter and a trough in summer. Relative velocity variations at higher frequencies show semiannual seasonal variations, with peaks around March and September for most of the stations. Different processes may explain the different velocity perturbations observed at low (0.2–0.5 and 0.5–1 Hz), intermediate (1–2 Hz), and high (2–8 Hz) frequencies.

Relative Velocity Variations as a Function of Noise Sources

The observed behavior may be related to seasonal changes in the subsurface but also to the well-known seasonal variations of the seismic noise sources (e.g., Meier *et al.*, 2010; Hobiger *et al.*, 2012). The noise levels recorded at any seismic station are related to different noise source processes. In our frequency bands of interest, secondary or double-frequency ocean microseisms are related to the dominant peak frequencies around 0.16 Hz, and they were explained by Longuet-Higgins (1950) as being generated by nonlinear pressure perturbations in the ocean bottom caused by the coupling of ocean waves of equal wavelengths traveling in opposite directions. High-frequency seismic noise ($f > 0.5$ Hz) may have natural causes such as wind (e.g., Withers *et al.*, 1996), but the dominant sources of high-frequency noise are man-made and significantly attenuated with depth. To check if our observations are related to the noise sources we investigated the seasonal variation of noise levels at the analyzed frequency bands.

Figure 7 (right) shows the evolution of the daily average PSD of seismic noise recordings at station PV01 for the 15-month time period considered in the analyzed frequency bands. A 30-day running average of the PSDs is also plotted in order to make a comparison with the relative velocity var-

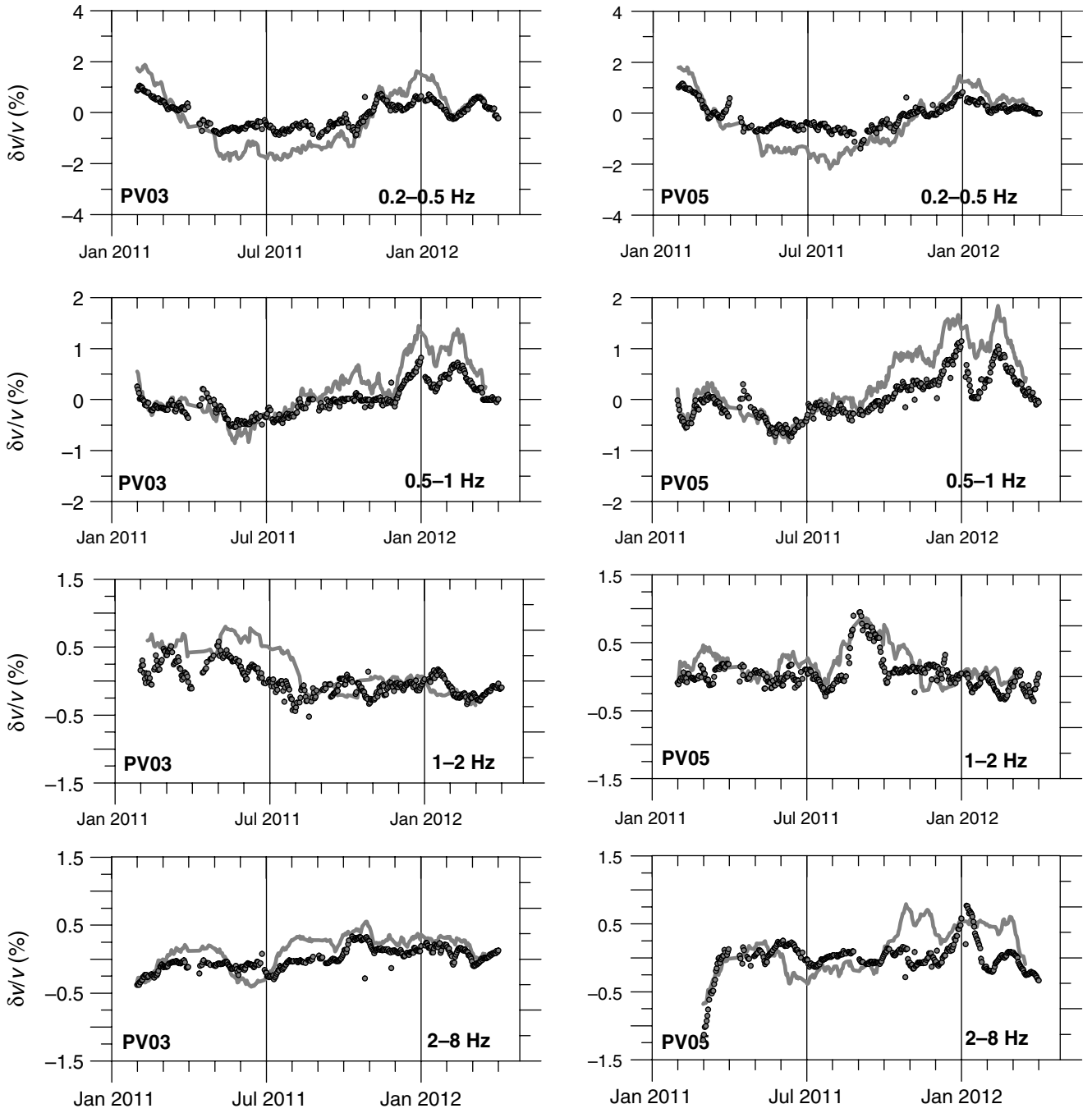

Figure 6. Relative velocity variations at stations PV03 and PV05 of the PV network for the studied frequency range in the period 1 January 2011 to 31 March 2012. The time length used for the ACF smoothing is 30 days. Results obtained using the stretching technique (gray solid line) and the MWCS method (gray dots) are plotted.

iations. The velocity trough in summer and peak in winter (Fig. 7a, left panel) are in phase with the dominant seasonal pattern of the PSD (Fig. 7a, right panel) for the 0.2–0.5 Hz frequency band. For higher frequencies, however, no clear correlation is observed between the velocity perturbations and the PSD variations. Zhan *et al.* (2013) pointed out that changes in the raw noise frequencies that are not removed in the preprocessing, including spectral whitening, may cause a temporal variability of the ACFs frequency content. To further examine the seasonal patterns observed, we plotted an example of the time variation of the amplitude spectra (a_p) and predominant frequency (f_p) of the ACFs, which are computed by Fourier transforming the 30-day stacked, band-pass-filtered ACFs, for the same time windows used for estimating the velocity variations (i.e., 10–25 s for 0.2–0.5 Hz; Fig. 8). The velocity changes computed at station

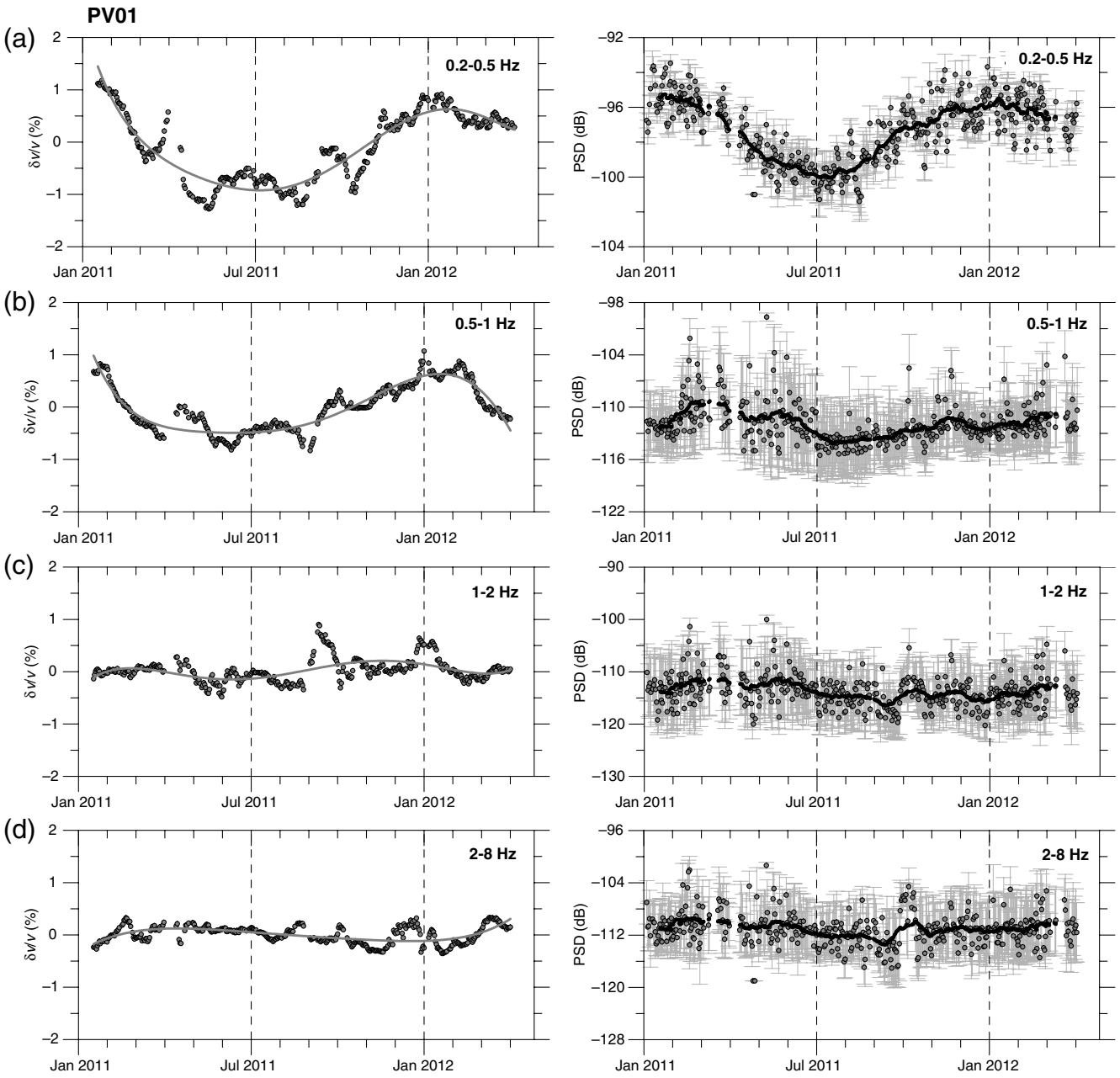

Figure 7. (a–d, left panels) Relative velocity variations at station PV01 for the studied frequency range using the MWCS technique; the gray solid line plots the long-term variation. (a–d, right panels) Amplitude of the PSD function of seismic noise and standard deviation at station PV01 for four frequency ranges from 0.2 to 8 Hz. The solid line is the 30-day data running average.

PV09 using the MWCS method for the 0.2–0.5 Hz frequency band are also plotted. For the 30-day stacked ACFs, f_p is constant for the analyzed time period (Fig. 8b); however, a_p presents a seasonal pattern that seems to correlate well with the velocity changes (Fig. 8a). This observation suggests the seasonal variations of the noise sources may explain the observed seasonal changes of seismic velocity in the lowest analyzed frequency band. Another way to infer the source directionality of ambient seismic noise would be to perform beamforming using data from a dense network or a seismic array (e.g., Rost and Thomas, 2002; Behr *et al.*, 2013).

Location of the Relative Velocity Changes

At short lapse times, it is expected that single scattering will dominate compared to multiple scattering (e.g., Sato and Fehler, 1998). Within this framework, the relative velocity variations estimated by means of PII using coda waves may be caused by velocity changes inside a volume bounded by the single scattering shell. In the case of collocated source and receiver, the scattering shell for single scattered surface waves is a circle with radius $vt/2$ and penetration depth of 0.4λ, in which λ is the wavelength (Lowrie, 2007). For a surface-wave velocity v of 2 km/s in the region and the consid-

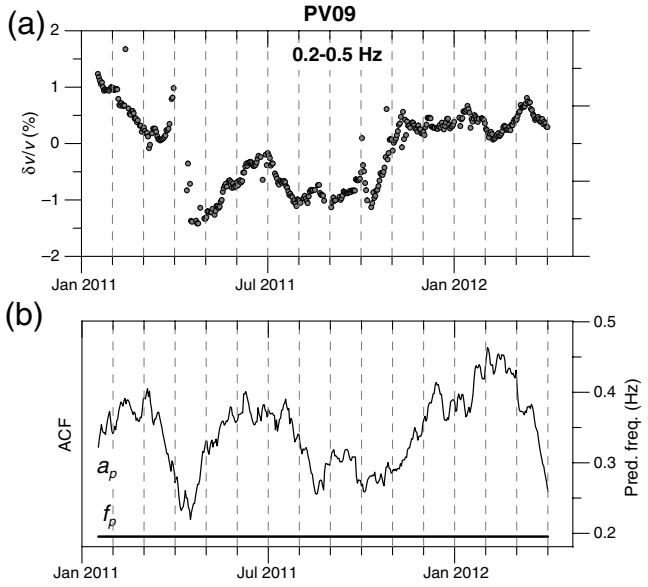

Figure 8. (a) Relative velocity variations at station PV09 using the MWCS technique; and (b) spectral amplitude and predominant frequency of the ACF for the 0.2–0.5 frequency range.

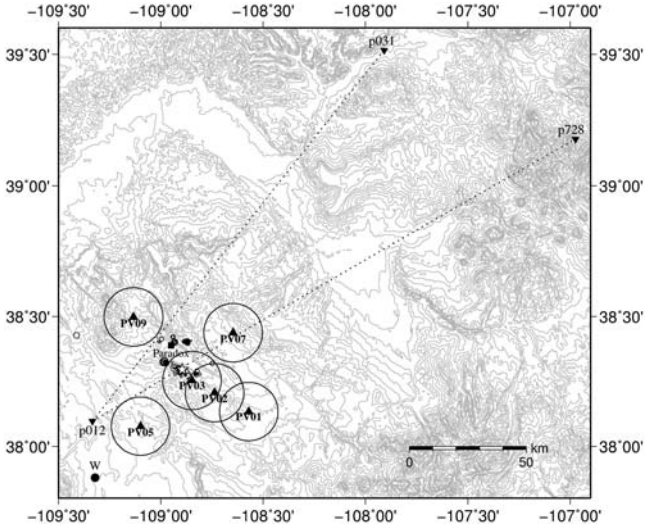

Figure 9. Areas sampled by coda waves in this study. The circles mark the 25 km radius single scattering shells around each seismic station. Epicenters of the induced earthquakes that occurred during 2011 are plotted with open circles. The open star marks the location of the deep injection well. The two dotted lines are the analyzed trajectories between Global Positioning System (GPS) stations p012-p031 and p012-p728. The location of the Paradox 2N meteorological station is also plotted. W marks the location of the water well. The map was drawn with Generic Mapping Tools (Wessel and Smith, 1998).

ered travel time from 10 to 25 s for the 0.2–0.5 Hz frequency band, it yields a region of radius 25 km, and a penetration depth of 4 km. For the higher analyzed frequency band (2–8 Hz) and taking into account the considered travel time from 1 to 2.5 s, the velocity changes may be located inside a region of radius 2.5 km with a depth of 400 m. If coda mainly consisted of *S* waves, the scattering shell would be a sphere of similar radius but deeper penetration depth. For large lapse times, multiple scattering would dominate in the coda. In the limit of strong multiple scattering, the diffusion approximation would be valid, and the sensitivity kernel of the ACF would be more local (e.g., Pacheco and Snieder, 2005). Figure 9 shows the largest regions sampled in this study for the analyzed stations of PV network according to the single scattering theory. The sampling regions for stations PV01, PV02, and PV03 overlay and PV03 samples the injection point area. Only PV02 and PV03 sample the region where induced earthquakes occurred during the analyzed time period.

Relative Velocity Variations and Crustal Deformations

In order to check for possible crustal deformations in the region that could be related to the observed velocity changes, we measured the differential baseline length of the horizontal displacements between two pairs of permanent Global Positioning System (GPS) stations across Paradox Valley region. For this purpose, we downloaded the time-series data from the Scripps Orbit and Permanent Array Center for three stations: p012, p031, and p728 (their locations are plotted in Fig. 9). The horizontal differential displacements with respect to a baseline for two pairs of GPS stations were computed for the analyzed 15-month period, and they are represented in Figure 10a,b together with the corresponding 30-day running average data plot. With the available data resolution, no horizontal displacement is recognized in this figure using GPS instruments. Only a seasonal variation is observed, which correlates well with the relative velocity changes and is temporally out of phase with the average surface temperature variations (Fig. 10c). The seasonal displacement of GPS data is usually attributed to several sources such as thermal and hydrodynamic effects. Prawirodirdjo *et al.* (2006) suggested that a large part of the annual variations in the horizontal position time series of GPS stations in southern California could be explained by thermoelastic strain induced by atmospheric temperature variations. Nevertheless, Tsai (2011) found that hydrologic loading, not thermoelastic displacements, can account for a significant fraction of the observed GPS signal and seismic-wave velocity variations in southern California. The possible sources of the seasonal variations observed in this work will be discussed in the next section.

Relative Velocity Variations Related to Hydrologic Loading

Variations in meteorological conditions such as temperature or precipitation may cause changes in the mechanical properties of the Earth's crust. Meier *et al.* (2010) found seasonal variations of travel-time perturbations within the Los Angeles basin and concluded they might be caused by changes in the groundwater aquifer or thermoelastic strain

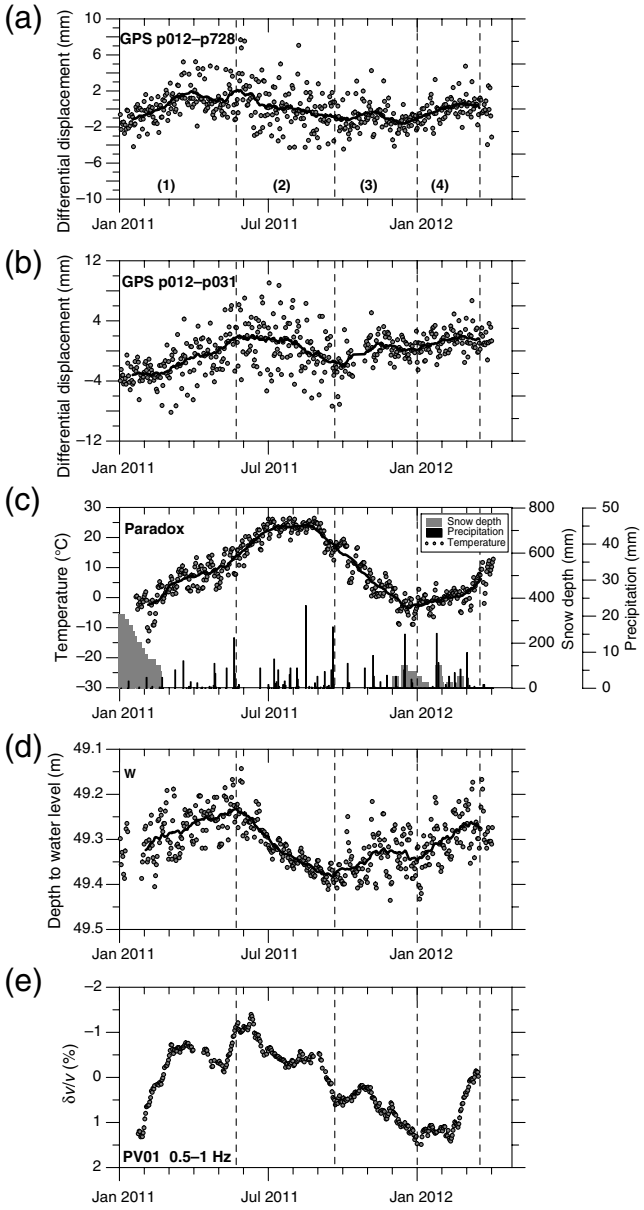

Figure 10. Comparison of the computed and recorded observables in the period 1 January 2011 to 31 March 2012. The solid lines are the computed 30-day data running average for each observable. (a) and (b) The measured horizontal differential displacements for the GPS stations pairs p012-p728 and p012-p031, respectively; (c) mean temperature, snow depth, and precipitation recorded at the Paradox 2N meteorological station; (d) depth to water level; and (e) relative velocity variation for station PV01 in the frequency band 0.5–1 Hz. Note the descending order of $\delta v/v$ in the left vertical axis.

variations. Following Tsai (2011), and according to our observations, the velocity and temperature changes do not have the right phase to be explained through thermoelastic variations in Paradox Valley. Velocity decrease induced by the effective stress diminishment due to increased pore pressure caused by infiltration of rainwater has been observed in other regions. Sens-Schönfelder and Wegler (2006) reported periods of decreasing velocities caused by rain-induced increases in groundwater level at Merapi volcano, Indonesia, using PII. Meier *et al.* (2010) also observed a velocity decrease at the beginning of the year after the rainy season in California, when the Los Angeles basin becomes most inflated according to GPS measurements and the aquifer should be at a maximum. Liu *et al.* (2013) have observed a correlation of seismic velocity changes with the water level variation at the Zipingpu reservoir, in the epicentral zone of the Wenchuan earthquake, with a reduction of the velocity when the water level is high. Ikuta *et al.* (2002) observed a velocity decrease arising from the increase in the groundwater level in Japan and concluded that long-term travel-time variations were mostly affected by rainfall. Clymer and McEvilly (1981) also reported increased travel times with the more shallow water level in California. They explained these measurements, which are in contrast with general laboratory observations of velocity increases upon saturation, as a combined effect of increased density and reduced shear modulus for the newly wetted medium. In order to perform a comparison with the variations of water table level in Paradox Valley, we downloaded the groundwater daily data from the USGS for one well in the study region (the location of the well is plotted in Fig. 9). Figure 10d shows the evolution of the depth to water table from 1 January 2011 to 31 March 2012. A good correlation of the differential displacement measured at the GPS stations (Fig. 10b,c) with the 30-day running average water level variations at the well can be observed. For a clear interpretation of the long-period relative velocity changes, we have divided the time axis into four segments. Time period 1 is characterized by a decreasing trend of the relative velocity and an increase of the water level. In time period 2, the relative velocity increases again, and the water level in the well decreases. Time period 3 shows a decrease and increase of the relative velocity, together with an increase and decrease of the water level. Finally, the decreasing trend of the relative velocity in time period 4 corresponds to an increase of the water level in the well. These observations let us conclude that hydrologic loading may explain a significant fraction of the annual relative velocity variations measured in this region.

Short-Term Relative Velocity Variations

Numerous studies have shown that seismic velocity is sensitive to the level of applied stress in the medium (e.g., Nur and Simmons, 1969; Yamamura *et al.*, 2003; Niu *et al.*, 2008). The precision at which seismic velocity variations can be estimated determines the precision to which stress changes can be identified. Rivet *et al.* (2011) detected a relative velocity change of the order of $\sim 10^{-3}$ with a stress sensitivity of the velocity change of 7×10^{-3} MPa^{-1} for a volumetric deformation of $\sim 10^{-6}$ associated with a slow-slip event in Mexico. Brenguier *et al.* (2008b) measured relative velocity perturbations of the order of -1×10^{-3}, which were related to an overpressure level of ~2 MPa in the Piton de la Fournaise volcano. Wegler *et al.* (2009) observed velocity

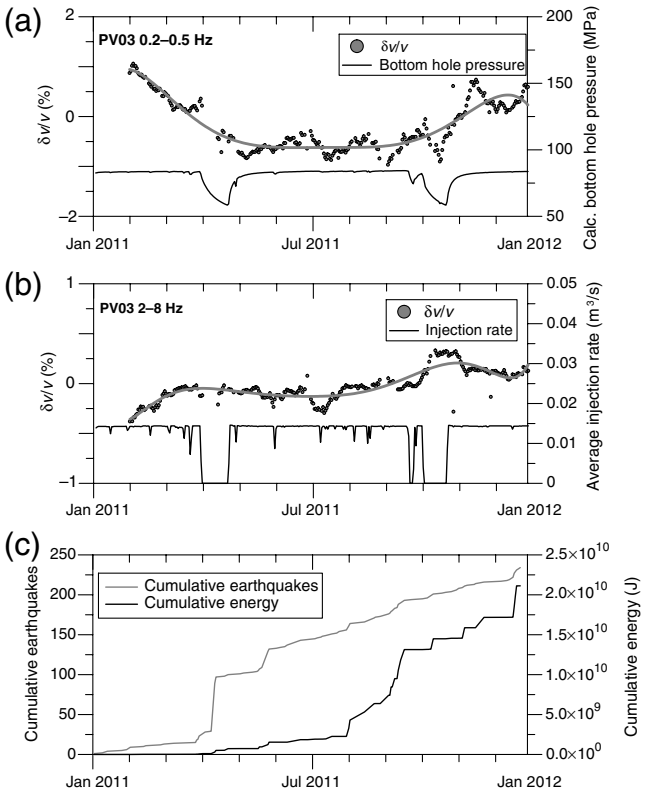

Figure 11. Comparison of observables for the year 2011. (a) Relative velocity for station PV03 in the frequency band 0.2–0.5 Hz using the MWCS method (the gray solid line is the computed long-term variation); and calculated bottom hole pressure at the injection well. (b) Relative velocity for station PV03 in the frequency band 2–8 Hz using the MWCS method (the gray solid line is the computed long-term variation); and average injection rate at the well; and (c) cumulative number of earthquakes and cumulative energy reported in the study area.

drops between −0.2% and −0.5% and computed volumetric strain changes at the free surface from -0.8×10^{-7} to 3.3×10^{-6} after the mid-Niigata earthquake in Japan. Mordret *et al.* (2010) found maximum relative velocity changes $\sim -0.8\%$ for an overpressure of ∼34 MPa with lack of observed ground deformation in Ruapehu volcano, New Zealand. Minato *et al.* (2012) obtained estimations of maximum areal strain changes of $\sim 1.2 \times 10^{-3}$ that correlated with velocity changes of $\sim -1.8\%$. Ueno *et al.* (2012) found a velocity decrease of more than 0.3% when the volumetric strain at the surface was larger than 10^{-6} during an earthquake swarm in Japan.

In Paradox Valley, the USBR injects brine 4.3–4.8 km below the surface to a deep limestone formation. This activity has resulted in several thousands of surface recorded seismic events since the start of the steady injection in 1996. Denlinger *et al.* (2010) studied the relationship between changes in local stress and seismicity in Paradox Valley and concluded that long-term injection has significantly altered the stresses within 3–4 km of the injection well. Roeloffs and Denlinger (2013) and Roeloffs *et al.* (2013) found shear stresses extending radially out to nearly 28 km from the well in Paradox Valley. As an example, Roeloffs and Denlinger (2013) simulated shear stresses of 0.04 MPa in the upper two kilometers of basement below the impermeable boundary and radial strains of the order $\sim 10^{-6}$ on the surface at 4 km from the injection well.

During 2011, more than 230 induced events with magnitudes ranging from −0.9 to 2.7 were reported in Paradox Valley area. Figure 11a,b shows the relative velocity variations obtained at station PV03, which is the closest site to the injection point, together with the cumulative number and energy of earthquakes occurred in the region during the year 2011 (Fig. 11c). In this figure, as well as for all the stations and studied frequency bands, there is not any observable signal above the background scatter that could be associated to the beginning of the active earthquake periods.

We also checked for possible changes in seismic velocities that could be associated with changes in fluid saturation and in pore pressure due to the injection process. Figure 11a,b plots the calculated bottom hole pressure and the average injection rates for the year 2011, together with the observed relative velocity variations in the frequency ranges 0.2–0.5 and 2–8 Hz. The lowest frequency band would have penetration depths of 4 km, whereas the injection is performed at depths up to 4.8 km. We are not able to recognize any signal in the relative velocity curves that would suggest a relationship with the injection activities.

Although the stress and strain changes that take place at Paradox Valley due to the injection process could be significant for our velocity variation measurements, detection of temporal changes is limited by the accuracy with which velocity measurements can be made. If the duration of any potential signal is less than 30 days, the averaging may suppress any signal, especially if it is weak. Moreover, only station PV03 is located close enough to the injection site, in consequence, more precise interpretations of the short-period relative velocity variations cannot be made in the Paradox Valley region until more high-quality seismic data are available.

Conclusions

We have computed the relative velocity variations at Paradox Valley through the analysis of the coda of the autocorrelation functions of seismic noise in four frequency bands from 0.2 to 8 Hz. Stability of the measurements is reached through a 30-day averaging of the ACFs. The most important feature observed is the clear seasonality of the relative velocity changes that show semiannual seasonal variations at higher frequencies and an annual period with a relative velocity peak in winter and trough in summer for the lower frequency bands.

Results suggest the directivity of noise sources may affect the long-term variations observed in the 0.2–0.5 Hz frequency band. For higher frequencies, hydrologic loading may explain a larger fraction of both the annual displacements measured with GPS data and the observed velocity variations.

No clear relationship between the short-term relative velocity variations and the occurrence of induced earthquakes and the fluid injection activity is found in this work. One of the reasons may be the present surface seismic network configuration, which may have limited use to detect changes due to injection. More high-quality data from a denser network would be also necessary to increase the temporal resolution. This would allow computation of the CCFs between station pairs and performance of a regionalization of the measurements that would facilitate a more detailed interpretation.

Data and Resources

Seismograms from the PV network used in this study were downloaded from the U.S. Geological Survey's National Earthquake Data Center. Metadata were obtained from Incorporated Research Institutions for Seismology (IRIS) Data Management Center (http://www.iris.edu; last accessed January 2013). Hourly surface meteorological data were provided by the U.S. National Climatic Data Center (http://www.ncdc.noaa.gov/cdo-web; last accessed February 2013) (DS3505—Surface Data, Hourly Global). Global Positioning System (GPS) data time series were downloaded from Scripps Orbit and Permanent Array Center (SOPAC) at http://sopac.ucsd.edu/ (last accessed February 2013). Groundwater daily data were obtained from http://waterdata.usgs.gov (last accessed March 2013). Elevation data was obtained from the National Elevation Dataset of the USGS at http://nationalmap.gov/elevation.html (last accessed May 2013).

Acknowledgments

We are very grateful to Lisa Block (U.S. Bureau of Reclamation) for providing us with valuable information and data from the Paradox Valley Unit. We also thank Diane Doser, Editor-in Chief, the Associate Editor Stefano Parolai, and two anonymous reviewers whose comments helped to improve this paper. This is a contribution of the Team Consolider-Ingenio 2010 TOPO-IBERIA (CSD2006-00041). Funds provided by REPSOL CO-DOS project support A. Ugalde and B. Gaite.

References

Ake, J., K. Mahrer, D. O'Connell, and L. Block (2005). Deep-injection and closely monitored induced seismicity at Paradox Valley, Colorado, *Bull. Seismol. Soc. Am.* **95,** 664–683, doi: 10.1785/0120040072.

Anggono, T., T. Nishimura, H. Sato, H. Ueda, and M. Ukawa (2012). Spatio-temporal changes in seismic velocity associated with the 2000 activity of Miyakejima volcano as inferred from cross-correlation analyses of ambient noise, *J. Volcanol. Geoth. Res.* **247/248,** 93–107, doi: 10.1016/j.jvolgeores.2012.08.001.

Behr, Y., J. Townend, M. Bowen, L. Carter, R. Gorman, L. Brooks, and S. Bannister (2013). Source directionality of ambient seismic noise inferred from three-component beamforming, *J. Geophys. Res.* **118,** 240–248, doi: 10.1029/2012JB009382.

Brenguier, F., M. Campillo, C. Hadziioannou, N. M. Shapiro, R. Nadeau, and E. Larose (2008a). Postseismic relaxation along the San Andreas fault at Parkfield from continuous seismological observations, *Science* **321,** 1478–1481, doi: 10.1126/science.1160943.

Brenguier, F., N. M. Shapiro, M. Campillo, V. Ferrazzini, Z. Duputel, O. Coutant, and A. Nercessian (2008b). Toward forecasting volcanic eruptions using seismic noise, *Nature Geosci.* doi: 10.1038/ngeo104.

Campillo, M., H. Sato, N. M. Shapiro, and R. D. van der Hilst (2011). New developments on imaging and monitoring with seismic noise, *C. R. Geosci.* **343,** 487–495, doi: 10.1016/j.crte.2011.07.007.

Chen, J. H., B. Froment, Q. Y. Liu, and M. Campillo (2010). Distribution of seismic wave speed changes associated with the 12 May 2008 M_w 7.9 Wenchuan earthquake, *Geophys. Res. Lett.* **37,** L18302, doi: 10.1029/2010GL044582.

Clarke, D., L. Zaccarelli, N. M. Shapiro, and F. Brenguier (2011). Assessment of resolution and accuracy of the Moving Window Cross Spectral technique for monitoring crustal temporal variations using ambient seismic noise, *Geophys. J. Int.* **186,** 867–882, doi: 10.1111/j.1365-246X.2011.05074.x.

Clymer, R. W., and T. V. McEvilly (1981). Travel-time monitoring with vibroseis, *Bull. Seismol. Soc. Am.* **71,** 1903–1927.

Denlinger, R. P., E. A. Roeloffs, and D. R. O'Conell (2010). Changes in seismicity and stress in response to fluid injection, Paradox Valley, Colorado, *Eos Trans. AGU* (Fall Meet.), Abstract #S13B–1999.

Duputel, Z., V. Ferrazzini, F. Brenguier, N. Shapiro, M. Campillo, and A. Nercessian (2009). Real time monitoring of relative velocity changes using ambient seismic noise at the Piton de la Fournaise volcano (La Réunion) from January 2006 to June 2007, *J. Volcanol. Geoth. Res.* **184,** 164–173, doi: 10.1016/j.jvolgeores.2008.11.024.

Hadziioannou, C., E. Larose, O. Coutant, P. Roux, and M. Campillo (2009). Stability of monitoring weak changes in multiply scattering media with ambient noise correlation: Laboratory experiments, *J. Acoust. Soc. Am.* **125,** no. 6, 3688–3695, doi: 10.1121/1.3125345.

Hobiger, M., U. Wegler, K. Shuiomi, and H. Nakahara (2012). Coseismic and postseismic elastic wave velocity variations caused by the Iwate-Miyagi Nairiku earthquake, Japan, *J. Geophys. Res.* **117,** no. B09313, doi: 10.1029/2012JB009402.

Ikuta, R., K. Yamaoka, K. Miyakawa, T. Kunitomo, and M. Kumazawa (2002). Continuous monitoring of propagation velocity of seismic wave using ACROSS, *Geophys. Res. Lett.* **29,** no. 13, doi: 10.1029/2001GL013974.

Larose, E., L. Margerin, A. Derode, B. van Tiggelen, M. Campillo, N. Shapiro, A. Paul, L. Stehly, and M. Tanter (2006). Correlation of random wavefields: An interdisciplinary review, *Geophysics* **71,** SI11–SI21, doi: 10.1190/1.2213356.

Liu, Z., J. Huang, Z. Peng, and J. Su (2013). Seismic velocity changes in the epicentral region of the 2008 Wenchuan earthquake measured from three-component ambient noise correlation techniques, *Geophys. Res. Lett.* doi: 10.1002/2013GL058682.

Lobkis, O., and R. Weaver (2003). Coda-wave interferometry in finite solids: Recovery of P-to-S conversion rates in an elastodynamic billiard, *Phys. Rev. Lett.* **90,** no. 254302, doi: 10.1103/PhysRevLett.90.254302.

Longuet-Higgins, M. D. (1950). A theory on the origin of microseisms, *Phil. Trans. Roy. Soc. Lond. A.* **243,** 1–35.

Lowrie, W. (2007). *Fundamentals of Geophysics* Second Ed., Cambridge University Press, New York, 375 pp.

Maeda, T., K. Obara, and Y. Yukutake (2010). Seismic velocity decrease and recovery related to earthquake swarms in a geothermal area, *Earth Planets Space* **62,** 685–691, doi: 10.5047/eps.2010.08.006.

Margerin, L., and H. Sato (2011). Reconstruction of multiply-scattered arrivals from the cross-correlation of waves excited by random noise sources in a heterogeneous dissipative medium, *Wave Motion* **48,** 146–160, doi: 10.1016/j.wavemoti.2010.10.001.

McNamara, D. E., and R. I. Boaz (2011). PQLX: A seismic data quality control system description, applications, and users manual, *U.S. Geol. Surv. Open-File Rept. 2010-1292*, 41 pp.

Meier, U., N. Shapiro, and F. Brenguier (2010). Detecting seasonal variations in seismic velocities within Los Angeles basin from correlations of ambient seismic noise, *Geophys. J. Int.* **181,** 985–996, doi: 10.1111/j.1365-246X.2010.04550.x.

Minato, S., T. Tsuji, S. Ohmi, and T. Matsuoka (2012). Monitoring seismic velocity change caused by the 2011 Tohoku-oki earthquake using ambient noise records, *Geophys. Res. Lett.* **39,** L09309, doi: 10.1029/2012GL051405.

Mordret, A., A. D. Jolly, Z. Duputel, and N. Fournier (2010). Monitoring of phreatic eruptions using interferometry on retrieved cross-correlation function from ambient seismic noise: Results from Mt. Ruapehu, New Zealand, *J. Volcanol. Geoth. Res.* **191,** 46–59, doi: 10.1016/j.jvolgeores.2010.01.010.

Niu, F., P. G. Silver, T. M. Daley, X. Cheng, and E. L. Majer (2008). Preseismic velocity changes observed from active source monitoring at the Parkfield SAFOD drill site, *Nature* **454,** 204–208, doi: 10.1038/nature07111.

Nur, A., and G. Simmons (1969). Stress-induced velocity anisotropy in rock: An experimental study, *J. Geophys. Res.* **74,** no. 27, 6667–6674.

Ohmi, S., K. Hirahara, H. Wada, and K. Ito (2008). Temporal variations of crustal structure in the source region of the 2007 Noto Hanto earthquake, central Japan, with passive image interferometry, *Earth Planets Space* **60,** 1069–1074.

Pacheco, C., and R. Snieder (2005). Time-lapse travel time change of multiply scattered acoustic waves, *J. Acoust. Soc. Am.* **118,** 1300–1310, doi: 10.1121/1.2000827.

Peterson, J. (1993). Observation and modeling of seismic background noise, *U.S. Geol. Surv. Open-File Rept. 1993-322*, 95 pp.

Poupinet, G., W. L. Ellsworth, and J. Fréchet (1984). Monitoring velocity variations in the crust using earthquake doublets: An application to the Calaveras fault, California, *J. Geophys. Res.* **89,** 5719–5731, doi: 10.1029/JB089iB07p05719.

Prawirodirdjo, L., Y. Ben-Zion, and Y. Bock (2006). Observation and modeling of thermoelastic strain in Southern California Integrated GPS Network daily position time series, *J. Geophys. Res.* **111,** no. B02408, doi: 10.1029/2005JB003716.

Rivet, D., M. Camplillo, N. M. Shapiro, V. Cruz-Atienza, M. Radiguet, N. Cotte, and V. Kostoglodov (2011). Seismic evidence of nonlinear crustal deformation during a large slow slip event in Mexico, *Geophys. Res. Lett.* **38,** L08308, doi: 10.1029/2011GL047151.

Roeloffs, E. A., and R. P. Denlinger (2013). Coupled deformation and flow modeling in the study of induced seismicity: An example from the Paradox basin, Colorado, *Geol. Soc. Am.* Annual Meeting, Paper No. 159–1.

Roeloffs, E. A., B. Ellworth, S. Hickman, O. Kaven, A. Llenos, A. McGarr, A. Michael, and J. Rubinstein (2013). U.S. Geological Survey earthquake research on injection-induced seismic activity: A progress report, in *Ground Water Protection Council (GWPC) 2013 Underground Injection Control Conference*, Sarasota, Florida, November 2013.

Rost, S., and C. Thomas (2002). Array seismology: Methods and applications, *Rev. Geophys.* **40,** no. 3, 1–27, doi: 10.1029/2000RG000100.

Sabra, K. G., P. Gerstoft, P. Roux, W. A. Kuperman, and M. C. Fehler (2005). Extracting time domain Green's function estimates from ambient seismic noise, *Geophys. Res. Lett.* **32,** L03310, doi: 10.1029/2004GL021862.

Sato, H. (2010). Retrieval of Green's function having coda waves from the cross-correlation function in a scattering medium illuminated by a randomly homogeneous distribution of noise sources on the basis of the first-order Born approximation, *Geophys. J. Int.* **180,** 759–764, doi: 10.1111/j.1365-246X.2009.04432.x.

Sato, H., and M. C. Fehler (1998). Seismic wave propagation and scattering in the heterogeneous earth, in *AIP Series in Modern Acoustics and Signal Processing*, Springer-Verlag, New York, 308 pp.

Sens-Schönfelder, C., and E. Larose (2008). Temporal changes in the lunar soil from correlation of diffuse vibrations, *Phys. Rev. E* **78,** no. 4, 045601, doi: 10.1103/PhysRevE.78.045601.

Sens-Schönfelder, C., and U. Wegler (2006). Passive image interferometry and seasonal variations of seismic velocities at Merapi volcano, Indonesia, *Geophys. Res. Lett.* **33,** L21302, http://dx.doi.org/10.1029/2006GL027797.

Sens-Schönfelder, C., and U. Wegler (2011). Passive image interferometry for monitoring crustal changes with ambient seismic noise, *C. R. Geosci.* doi: 10.1016/j.crte.2011.02.005.

Shapiro, N. M., and M. Campillo (2004). Emergence of broadband Rayleigh waves from correlations of the ambient seismic noise, *Geophys. Res. Lett.* **31,** L07614, doi: 10.1029/2004GL019491.

Shapiro, N. M., M. Campillo, L. Stehly, and M. H. Ritzwoller (2005). High-resolution surface-wave tomography from ambient seismic noise, *Science* **307,** 1615–1618, doi: 10.1126/science.1108339.

Snieder, R. (2006). The theory of coda wave interferometry, *Pure Appl. Geophys.* **163,** 455–473.

Tsai, V. (2011). A model for seasonal changes in GPS positions and seismic wave speeds due to thermoelastic and hydrologic variations, *J. Geophys. Res.* **116,** no. B04404, doi: 10.1029/2010JB008156.

Ueno, T., T. Saito, K. Shiomi, B. Enescu, H. Hirose, and K. Obara (2012). Fractional seismic velocity change related to magma intrusions during earthquake swarms in the eastern Izu peninsula, central Japan, *J. Geophys. Res.* **117,** no. B12305, doi: 10.1029/2012JB009580.

Ugalde, A., A. Villaseñor, B. Gaite, S. Casquero, D. Martí, A. Calahorrano, I. Marzán, R. Carbonell, and A. Pérez Estaún (2013). Passive seismic monitoring of an experimental CO2 geological storage site in Hontomín (Northern Spain), *Seismol. Res. Lett.* **84,** 75–84, doi: 10.1785/0220110137.

United States Bureau of Reclamation (2012). Review of geologic investigations and injection well site selection, Paradox Valley Unit, Colorado, *U.S. Bureau of Reclamation Technical memorandum n. 86-68330-2012-27*, 65 pp.

Wapenaar, K., and J. Fokkema (2006). Green's function representations for seismic interferometry, *Geophysics* **71,** no. 4, SI33–SI46.

Wapenaar, K., D. Draganov, R. Snieder, X. Campman, and A. Verdel (2010). Tutorial on seismic interferometry. Part 1: Basic principles and applications, *Geophysics* **75,** 75A195–75A209.

Wegler, U., and C. Sens-Schönfelder (2007). Fault zone monitoring with passive image interferometry, *Geophys. J. Int.* **168,** 1029–1033, doi: 10.1111/j.1365-246X.2006.03284.x.

Wegler, U., H. Nakahara, C. Sens-Schönfelder, M. Korn, and K. Shiomi (2009). Sudden drop of seismic velocity after the 2004 M_w 6.6 mid-Niigata earthquake, Japan, observed with passive image interferometry, *J. Geophys. Res.* **114,** no. B06305, doi: 10.1029/2008JB005869.

Wessel, P., and W. H. F. Smith (1998). New, improved version of Generic Mapping Tools released, *Eos Trans. AGU* **79,** no. 47, 579–579, doi: 10.1029/98EO00426.

Withers, M. M., R. C. Aster, C. J. Young, and E. P. Chael (1996). High-frequency analysis of seismic background noise as a function of wind speed and shallow depth, *Bull. Seismol. Soc. Am.* **86,** 1507–1515.

Yamamura, K., O. Sano, H. Utada, Y. Takei, S. Nakao, and Y. Fukao (2003). Long-term observation of in situ seismic velocity and attenutiaon, *J. Geophys. Res.* **108,** no. B6, 2317, doi: 10.1029/2002JB002005.

Zhan, Z., V. C. Tsai, and R. W. Clayton (2013). Spurious velocity changes caused by temporal variations in ambient noise frequency content, *Geophys. J. Int.* **194,** 1574–1581, doi: 10.1093/gji/ggt170.

Zhou, R., L. Huang, J. T. Rutledge, M. Fehler, T. M. Daley, and E. L. Majer (2010). Coda-wave interferometry analysis of time-lapse VSP data for monitoring geological carbon sequestration, *Int. J. Greenhouse Gas Control* **4,** 679–686, doi: 10.1016/j.ijggc.2010.01.010.

Institute of Earth Sciences Jaume Almera—CSIC
Lluís Solé i Sabarís s/n
08028 Barcelona, Spain
augalde@ictja.csic.es
bgaite@ictja.csic.es
antonio@ictja.csic.es

Manuscript received 21 May 2013;
Published Online 6 May 2014